Calibration of Airframe and Occupant Models for Two Full-Scale Rotorcraft Crash Tests

Martin S. Annett
Structural Dynamics Branch
NASA Langley Research Center
Hampton, VA 23681
martin.s.annett@nasa.gov

Lucas G. Horta
Structural Dynamics Branch
NASA Langley Research Center
Hampton, VA 23681
lucas.g.horta@nasa.gov

Michael A. Polanco
ATK Space Systems
Hampton, VA 23681
michael.a.polanco@nasa.gov

ABSTRACT

Two full-scale crash tests of an MD-500 helicopter were conducted in 2009 and 2010 at NASA Langley's Landing and Impact Research Facility in support of NASA's Subsonic Rotary Wing Crashworthiness Project. The first crash test was conducted to evaluate the performance of an externally mounted composite deployable energy absorber under combined impact conditions. In the second crash test, the energy absorber was removed to establish baseline loads that are regarded as severe but survivable. Accelerations and kinematic data collected from the crash tests were compared to a system integrated finite element model of the test article. Results from 19 accelerometers placed throughout the airframe were compared to finite element model responses. The model developed for the purposes of predicting acceleration responses from the first crash test was inadequate when evaluating more severe conditions seen in the second crash test. A newly developed model calibration approach that includes uncertainty estimation, parameter sensitivity, impact shape orthogonality, and numerical optimization was used to calibrate model results for the second full-scale crash test. This combination of heuristic and quantitative methods was used to identify modeling deficiencies, evaluate parameter importance, and propose required model changes. It is shown that the multi-dimensional calibration techniques presented here are particularly effective in identifying model adequacy. Acceleration results for the calibrated model were compared to test results and the original model results. There was a noticeable improvement in the pilot and co-pilot region, a slight improvement in the occupant model response, and an over-stiffening effect in the passenger region. This approach should be adopted early on, in combination with the building-block approaches that are customarily used, for model development and test planning guidance. Complete crash simulations with validated finite element models can be used to satisfy crash certification requirements, thereby reducing overall development costs.

1. INTRODUCTION

Efforts are underway within the rotorcraft community to develop comprehensive crash design criteria that encompass a wide range of rotorcraft classes, types, and configurations, and operating conditions. For the military, the standard for light fixed wing and rotary wing crash resistance [1] details seven crash impact design scenarios and specifies occupant seat acceleration limits and occupied volume reduction constraints. These design conditions are intended to encompass all weight classes and account for only two impact surfaces, rigid and plowed soil.

New standards have been proposed to replace specifications such as MIL-STD-1290A [2]. Essential in this effort is the development and assessment of modeling tools that can accurately associate impact velocities, attitudes and terrains to seat interface and occupant G-loads. Ultimately, crash safety certification by analysis is sought to lessen the necessity for costly full-scale crash tests. As the technology evolves to efficiently incorporate more modeling and simulation into the design process, next

Presented at the American Helicopter Society 68th Annual Forum, Fort Worth, TX, May 1-3, 2012.

generation rotorcraft will include more crashworthy features without sacrificing performance and minimizing weight.

Recent advancements in computational techniques have allowed for streamlined and efficient evaluations of the crash performance of rotorcraft. Finite element models have been developed that contain sufficient fidelity to model plastic deformation within the airframe during impact and are yet computationally affordable. Detailed representations of seats, occupants, and restraints are included to account for the load transfer between the airframe and the occupant and to directly assess the likelihood of occupant injury.

Allowing for increasingly complex models does not guarantee the accuracy of their predictions. Foremost to the development of any impact finite element model is the process of verification and validation [3]. Verification of models involves determining if the mathematical realization of the equation of motion is accurately implemented. Impact dynamics analyses typically rely on commercial finite element codes. Therefore, it is assumed that verification of the code is accounted for by the code vendor.

The validation phase involves ensuring that the physics of the problem agrees with the problem at hand, and establishing confidence that model results accurately represent physical behavior over an applicable domain. Model uncertainty must be quantified against the experimental data and must be consistent across the applicable domain. Full-scale impact tests are costly and infrequently conducted; therefore, identification of valuable validation metrics becomes vital.

Typically, validation comparisons between test and analysis are both qualitative and quantitative. One qualitative approach, only possible by the use of high-fidelity finite element models, is to compare post-impact airframe deformations and regions of damage. Quantitatively, the assertion of a properly validated model can be made by comparing error in kinematic responses such as position, velocity, or pitch angle. Any discernible differences that do exist between test and analysis require identifying and adjusting parameters within the model, and kinematic responses alone may not provide enough insight to guide adjustment. Output time history responses such as acceleration, velocity, strain, and pressure are then compared between sensor locations and their respective model nodes or elements. Relative errors for magnitude, time of arrival, and pulse duration can be used to compute comparison metrics such as Sprague and Geers [4] and Russell [5]. These metrics can reinforce model adequacy if acceptance criteria is satisfied, but they provide minimal guidance into required modifications to model parameters in the case of significant discrepancies.

Model calibration, or model updating, is undertaken throughout the verification and validation process to infer model parameters which would improve the agreement between the analysis and test results. Calibration based on one set of test data does not imply validation over the applicable design space. With additional test results, it can be demonstrated that model calibration successfully validates the model.

Test and analysis acceleration responses often contain high frequency content, particularly for thin walled airframe components under severe impact conditions. Correlating individual time-history magnitudes and durations becomes challenging and ambiguous. Low-pass filtering results may obscure deficiencies in the model that would need to be improved to reconcile test with analysis. An approach is desired that reveals both the temporal and spatial distribution of acceleration responses, taking advantage of the wealth of instrumentation available in full-scale tests. The approach initially discussed by Horta in [6] is used when calibrating specific airframe parameters to crash test results.

In the following sections, the experimental program and finite element model validation and calibration efforts will be discussed. Airframe calibration is conducted based on results from the second full-scale crash test. An independent calibration effort has been performed for the model of a Hybrid III Anthropomorphic Test Device (ATD) [7]. A series of rigid seat drop tests with Hybrid II and Hybrid III ATD's were used to improve model responses in the pelvic region of the Hybrid III FEM. The fully calibrated model is executed for both crash test conditions, encompassing a design space and loading that extends from low to severe.

2. FULL-SCALE TEST ARTICLE DESCRIPTION

Detailed descriptions of the full-scale crash tests of the MD-500 helicopter are provided in [8]. Testing was conducted at NASA Langley's Landing and Impact Research Facility in December 2009 and March 2010. Figure 1 shows the facility and a notional schematic of a swing test. Targeted impact conditions were 26-ft/sec vertical and 40-ft/sec horizontal while maintaining zero pitch, roll, and yaw

attitude. The test was conducted by suspending the helicopter from the gantry structure using two sets of cables: pullback cables and swing cables. These cables were attached to the airframe at hard points that enable the helicopter to be lifted through its center of gravity. During the test, the airframe was lifted using the pullback cables to a specified height and pyrotechnically released following a countdown. Swing cables were configured to form a parallelogram to minimize pitch angular velocity during the pendulum swing prior to impact. Just prior to ground contact, the supporting cables were pyrotechnically separated.

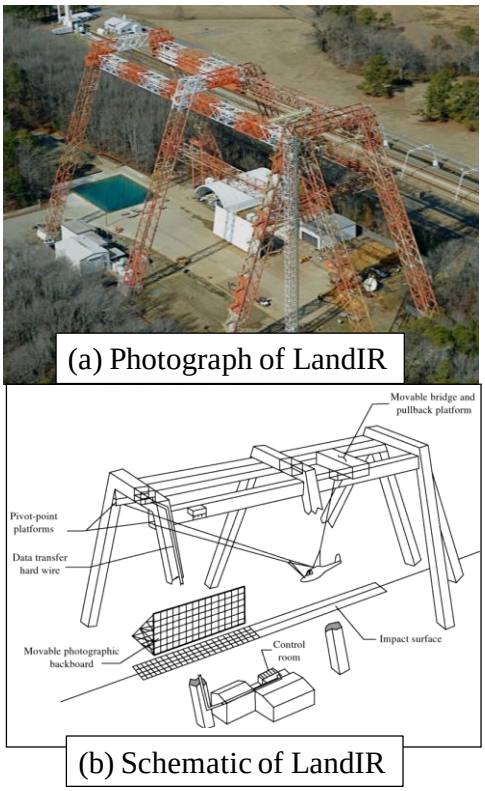

Figure 1. Landing and Impact Research Facility

A photograph of the MD-500E helicopter, manufactured by MD Helicopters, Inc. of Mesa Arizona, is shown in Figure 2a. Currently, the MD-500E is used as a general-purpose utility and executive transport helicopter for both military and civilian applications. The MD-500 helicopter is designed to seat four occupants, two crew and two passengers. The test article is shown in Figure 2b. Occupants were placed in standard seats and restrained using four-point harnesses for the crew and three point harnesses for the passengers. Seats consisted of a framework of aluminum tubing and nylon mesh fabric stretched over the frames to form a seat pan and seat back.

The target mass for the test article was set to 2,900 lb, which is roughly equal to the maximum gross takeoff weight for the MD-500E. Ballast mass was distributed onto the test article by adding steel tubing for swing cabling fixtures, steel plates and tubing to represent rotor and tail mass, and data acquisition support hardware to represent the transmission. Sand bags were placed in the subfloor region to account for fuel mass. The total weights of the test article with and without the DEA were 2,940 lb and 2,906 lb, respectively.

(a) MD-500E helicopter

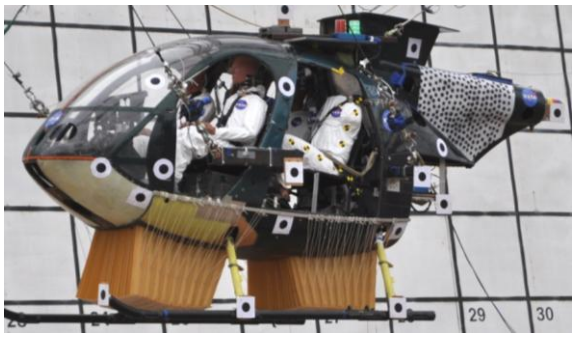

(b) MD-500 Crash Test Article with 2 DEA Blocks Attached

Figure 2. MD-500

Four instrumented ATD's were used to represent two crew and two passengers. The pilot in the front left crew position was a 50th percentile Hybrid III male ATD with a straight lumbar spine similar to the Hybrid II. The co-pilot in the front right crew position was a 50th percentile Hybrid II male ATD, and the rear passenger on the left side was a 50th percentile Hybrid II male ATD. The Hybrid II and III ATDs weigh 180 lb. For the right rear passenger a specialized Human Surrogate Torso Model (HSTM) developed by The Johns Hopkins University Applied Physics Laboratory (APL) was used [9]. This

biofidelic HSTM contains detailed representations of thoracic organs, skeletal structure, and soft tissue and is mated to the pelvis and legs of a 50th percentile Hybrid III male ATD. The weight of the HSTM/Hybrid III ATD is 170 lb.

The critical component evaluated in the first impact test was the externally mounted Kevlar/Epoxy Deployable Energy Absorber (DEA) [10]. The flexible honeycomb design allows for the DEA to be stowed flat external to the fuselage belly and deployed forming the hexagonal cell walls as notionally shown in Figure 3a. In this configuration, the DEA is loaded along the stiff cell axis causing the cell to permanently deform under load and thereby absorb energy. The cell walls fold to form a controlled accordion-like pattern (see Figure 3b). The effectiveness of the DEA was evaluated using a building-block approach beginning with material coupon static tests, progressing to sub-component static and dynamic tests, and culminating with the full-scale crash tests.

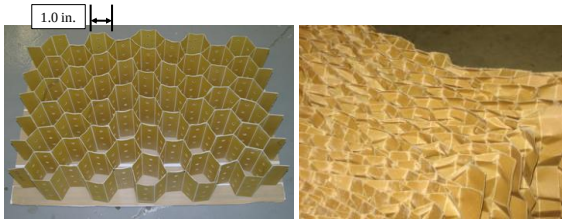

(a) DEA in deployed configuration (b) Post-impact DEA deformation

Figure 3. DEA

The fuselage and skid gear were instrumented with a combination of strain gages and accelerometers. ATD instrumentation included head, chest, and pelvic accelerometers, lumbar load cells, restraint load cells, and pressure gages. A total of 160 channels of data were collected at a sample rate of 10,000 Hz. In addition, measurements of vehicle kinematics were taken using two and three dimensional photogrammetry.

3. FULL SCALE CRASH TEST RESULTS

A detailed description of the test results is provided in [8]. The impact conditions for the two full-scale helicopter tests are summarized in Table 1. Note that the pitch and yaw attitudes for the first test were off-nominal. It was determined that the variations in the distribution of swing cable tension loads prior to release introduced rotational motion upon release. Several pre-lift tests were conducted prior to the second full-scale crash test to determine proper alignment procedures for cable loads which resulted in impact conditions closer to nominal.

Table 1. Full-Scale Test Impact Conditions

Test Parameters		Nominal Conditions	MD-500 with DEA	MD-500 Without DEA
Vehicle Weight (lb)		2,900	2,940	2,906
Linear Velocity (ft/sec)	**Long.**	40.	38.8	39.1
	Vert.	26.	25.6	24.1
	Lat.	0	0.5	0.6
Attitude (deg)	**Pitch**	0	-5.69	-6.2
	Roll	0	7.04	1.9
	Yaw	0	9.3	2.1
Angular Velocity (deg/sec)	**Pitch Rate**	0	0.44	0.54
	Roll Rate	0	1.11	0.68
	Yaw Rate	0	4.82	1.65

Figure 4 shows test sequence photos for the crash test with the DEA. Picture 1 shows the helicopter approximately 30 ms before impact, pitched down and with some slight yaw. Picture 2 shows the helicopter at the point of first skid gear impact when the right gear touches the ground. Picture 3 shows the point of maximum DEA crushing, and picture 4 shows post-impact rebound. The front right skid gear impacted the ground first, which was caused by the yaw and roll introduced during the swing. At the point of maximum crushing of the DEA (picture 3), the helicopter straightened out to show almost no pitch. After the point of maximum crush, the nose pitched forward on rebound, and the Hybrid ATD heads and torsos flailed forward and to the left.

Overall, the damage to the test article was minor. Impact occurred initially on the front right skid gear. Slight tears in the skin above the fuselage opening were evident for both skid gears. The DEA restraint support rail impeded the gear from additional movement with the result that the right gear bent along the rail. Damage along the fuselage belly was limited to the right front section of the belly forward of the front bulkhead. The subfloor and airframe were considered intact, and minimal repair work was required on the forward keel beam and belly to prepare the test article for the destructive crash test without DEA.

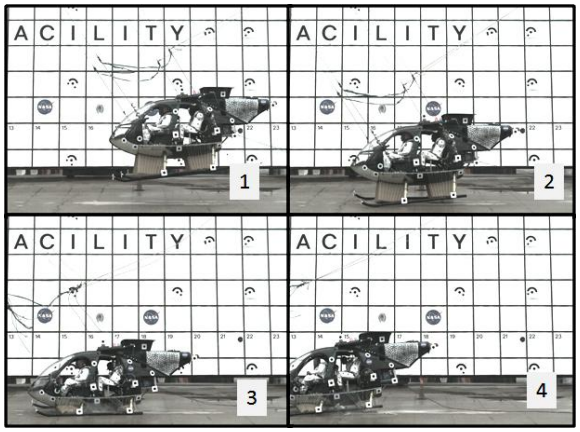

Figure 4. Test sequence from south camera, crash test with DEA

Figure 5 shows a sequence of photos for the test without the DEA. Picture 1 shows the helicopter before impact. Picture 2 shows the helicopter at the point of first skid gear impact. As with the MD-500 crash test without DEA, the right gear impacted the ground first, but the amount of yaw and roll was lower than the test with the DEA. The fuselage belly impacted the ground approximately 80 ms after gear impact, and the highest vertical deceleration loads were seen thereafter. Picture 3 shows the point of maximum vertical displacement, where the helicopter maintained a slight nose down pitch. Picture 4 shows minor post-impact rebound. After the point of maximum subfloor deformation, the nose pitched forward on rebound, and flailing of the ATD heads and torsos occurred.

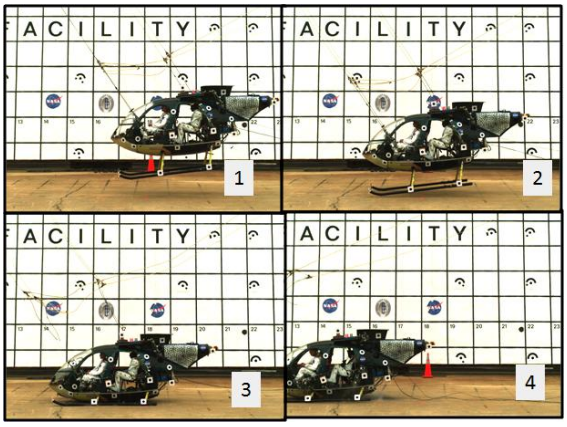

Figure 5. Test sequence from south camera, crash test without DEA

4. BASELINE LS-DYNA MODEL DESCRIPTION

The explicit finite element analysis program LS-DYNA was used to perform analyses [11]. A full description of the development of the system-integrated LS-DYNA FEM for the MD-500, shown in Figure 6, is included in [12]. A computer-aided design model of the MD-500 fuselage was provided by the U. S. Army Aviation Technology Directorate and consisted of surface representations of the fuselage, bulkheads, seat pans, and floor. Additionally, the skid gear, subfloor, and secondary frames and stiffeners were modeled from hand measurements. The crew and passenger seats were modeled with target tracking 3-D photogrammetric techniques in which photogrammetric point clouds were converted to parametric surfaces and finite element meshes.

The MD-500 FEM with the DEA has approximately 400,000 elements in total, with 266,000 elements representing the DEA. This model size is commensurate with automotive crash model sizes. Tradeoffs are continually considered when refining models that use explicit finite element techniques, where stability is conditionally enforced if the time steps are sufficiently small. The time step is a function of the shortest element dimension; therefore, for more refined meshes, the time steps decrease and overall runtime increases. Mass scaling was introduced to control the minimum time step. By increasing the masses of small elements without affecting the overall mass, the runtime can be shortened.

The FEM is primarily composed of shell elements, representing airframe skins, frames, stiffeners, skid gear, and DEAs. Material properties for the fuselage are based on the MD-500 Structural Repair Manual [13]. Crush tube struts are used to attach the skid gear to the fuselage and to distribute the landing and impact loads. These tube struts are modeled as one-dimensional spring elements that transmit axial loads and bending moments. Ballast and non-structural components are represented in the FEM with concentrated mass elements.

Figure 6. LS-DYNA FEM

A schematic of the shell-based DEA model is illustrated in Figure 7a. Convergence studies reported in [14] revealed that the maximum acceptable DEA element edge length was approximately 0.3 inches to replicate the folding patterns accurately. The material model is elastic and piecewise linear plastic with a Young's Modulus of 340,000 psi and initial yield stress of 7,500 psi. The yield stress versus plastic strain curve is plotted in Figure 7b.

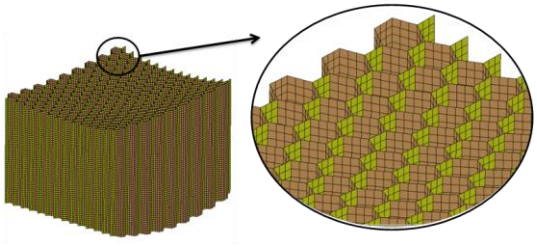

(a) Shell Based DEA FEA

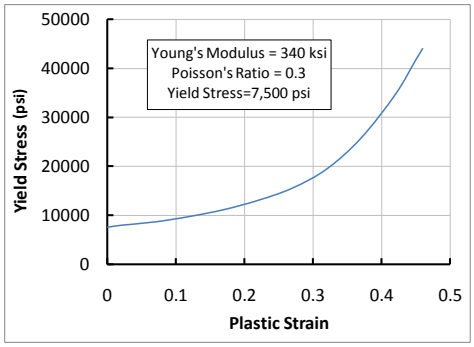

(b) DEA Material Properties

Figure 7. DEA FEM

A model of the 50th percentile Hybrid III male, denoted as the LSTC Hybrid III FEM [15], was used for the Hybrid II and III ATDs (Figure 8a). These models contain mostly rigid representations of the ATD components. However, the ribcage, neck, jacket, and pelvis are deformable. Springs and dampers were used in the neck and limb joints to model flexibility. To position the ATD, the FEMs were imported using the pre-processor LS-PREPOST. The LSTC Hybrid III FEM contains 4,295 elements.

The Hybrid II and III ATDs used in the crash tests are notably different than what is characterized with the LSTC Hybrid III FEM. The LSTC Hybrid III FEM has been calibrated for automotive frontal impact conditions, with emphasis on capturing head/neck and chest kinematics. For testing in aerospace applications, the Hybrid II and III ATDs contain straight lumbar spines, whereas the LSTC Hybrid III FEM includes the automotive curved spine. Moreover, the LSTC Hybrid III FEM does not contain an abdominal insert, which is a load path between the pelvis and lower ribcage under high vertical loading. Therefore, it is understood that the internal responses of the pelvic and lumbar region with the LSTC Hybrid III FEM are not accurate. Results reported in [7] support this finding. The mass distribution of the LSTC Hybrid III FEM is accurate provided there is limited torso flail during the initial impact. The LSTC Hybrid III FEM captures ATD/seat impact and its subsequent rebound and effective mass decoupling, and is therefore an upgrade over simply using lumped mass representations.

A reduced human torso FEM was constructed and adapted from APL's detailed Human Torso Finite Element Model (HTFEM) [9]. The reduced HTFEM was attached to the LSTC Hybrid III FEM pelvis and legs. The reduced HTFEM is depicted in Figure 8b. The pilot and co-pilot FEMs are restrained with four-point harnesses, and the passenger FEM and reduced HTFEM are restrained with three-point harnesses. Seatbelt shell elements were contoured to the torso and pelvis.

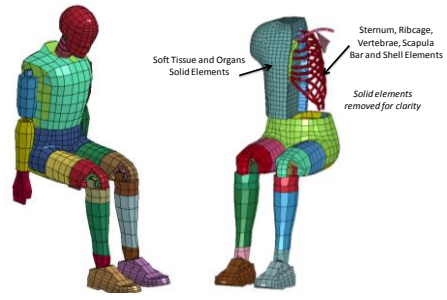

(a) LSTC Hybrid III FEM (b) Reduced HTFEM

Figure 8. ATD FEM's

5. TEST/ANALYSIS RESULTS- CRASH TEST WITH DEA

The test impact orientation and deformation at peak load is shown for test and analysis in Figure 9. Qualitatively, the global deformation pattern of the deployable energy absorber is similar to the deformation observed from the high speed video, primarily folding on the right side and crushing on the left side. Consequently, higher impact loads were transferred at locations where the DEA cells simply buckled. However, because damage to the front right side was not evident in the analysis, these regions of folding and crushing do not correspond between test and analysis. Within the simulation, dimpling of the skin occurred in the region above the rear DEA, whereas the post-test inspection revealed no damage. The indiscriminate behavior of DEA folding, crushing and sliding along the belly was due to the presence of lateral and longitudinal loading and was only partly captured with the shell-based DEA model.

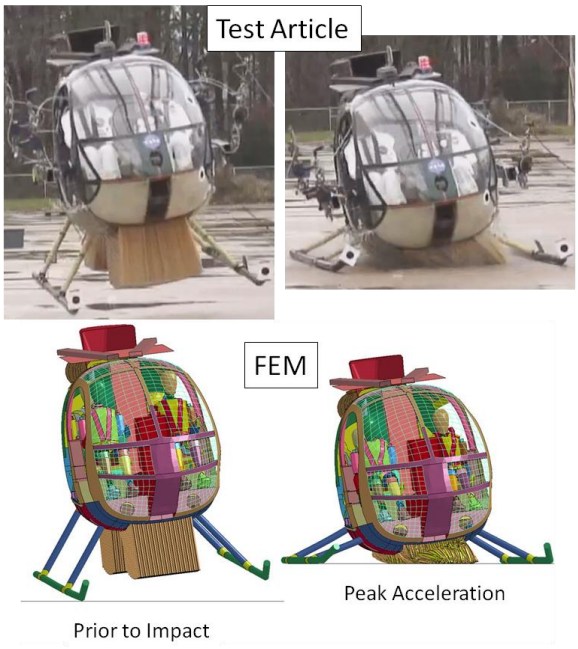

Figure 9. MD-500 FEM deformation, crash test with DEA

Despite the qualitative differences between local deformation patterns, the overall response of the airframe is in reasonable agreement. Nodal accelerations at two critical locations, the pilot seat box and the centerline of the floor beneath the passenger seats, are compared to accelerometer output. The reference coordinate system for the simulation and the test are fixed along the floor surface. The axis perpendicular to the floor represents the vertical direction. For purposes of evaluation of occupant injury criteria such as Eiband, Dynamic Response Index, and Brinkley [16-18], the responses for the pilot seat box and passenger floor are used as inputs.

The pilot seat box vertical accelerations are plotted in Figure 10, and the passenger floor accelerations in Figure 11. The data comparisons are plotted for 0.2 seconds. All acceleration data are low-pass filtered with a second-order Butterworth 60 Hz filter. As expected, the vertical acceleration responses of the airframe are effectively trapezoidal with durations of roughly 0.12 seconds. Note that the DEA performs as a load-limiting shock absorber, regulating the loads between 10 and 15 g and lengthening the duration of the imparted loads through crushing and folding. Because the airframe rebounded before full compaction of the DEA could occur, only a slight increase in the imparted load was observed.

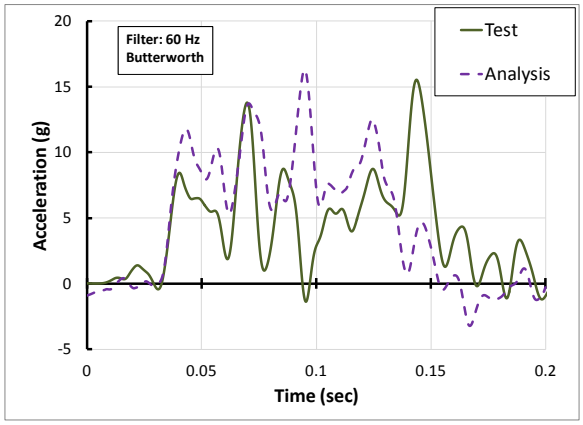

Figure 10. Comparison of test and analysis, pilot seat box vertical acceleration, crash test with DEA

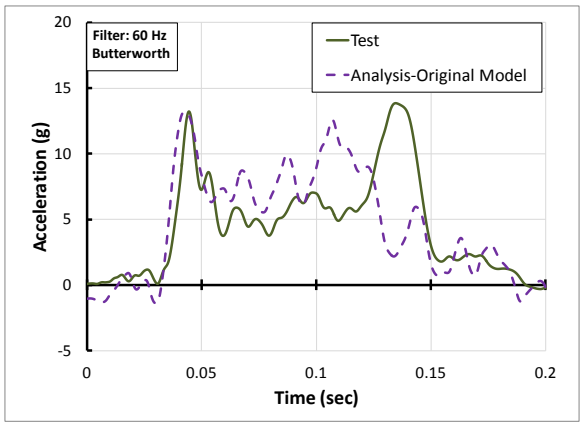

Figure 11. Comparison of test and analysis, passenger floor vertical acceleration, crash test with DEA

The pilot pelvic vertical acceleration is plotted in Figure 12. The peak acceleration from the analysis is over twice that seen in the test and the pulse shape is also different. These results provided the first indication that the ATD models were not specifically calibrated for the dominant vertical loading environments experienced in a rotorcraft crash.

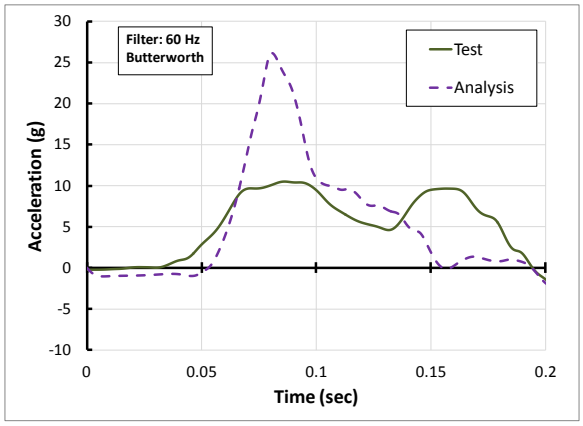

Figure 12. Comparison of test and analysis, pilot pelvis vertical acceleration, crash test with DEA

6. TEST/ANALYSIS RESULTS- CRASH TEST WITHOUT DEA

The test impact orientation and deformation at peak load is shown for test and analysis in Figure 13. Initial runs of the system integrated FEM following the crash test without the DEA revealed key shortcomings in the FEM that were not evident when validating against the crash test with DEA. During the test, much of the subfloor secondary structure, including the keel beam and frames, exhibited structural failure. Pilot and co-pilot seat boxes were permanently deformed, and seat frames either buckled or failed in bending. The tail deformed significantly, and the forward swing cable fixture became dislodged at its interface to the bulkhead. Acceleration magnitudes increased by a factor of three, and pulse durations were reduced to around 0.040 seconds. The pulses were triangular in shape, but contained different peaks depending on airframe location.

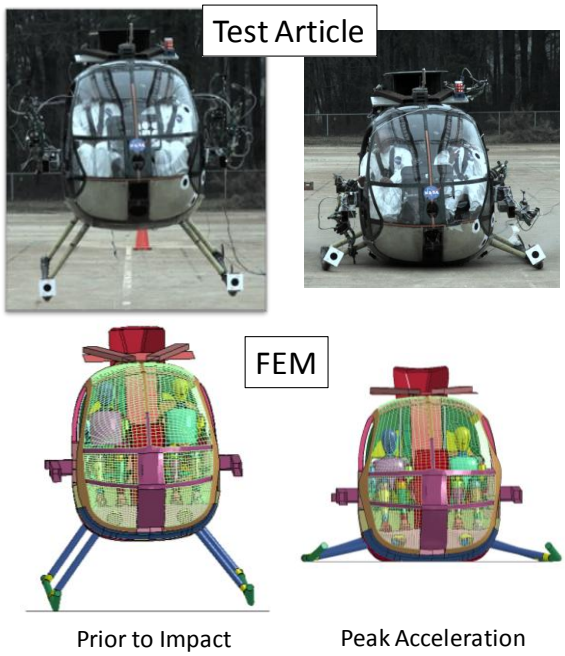

Figure 13. MD-500 FEM deformation, crash test without DEA

Results from the airframe FEM showed that the subfloor mesh was too coarse to accurately capture the keel beam and subfloor frame deformation. The predicted tail deformation was overly compliant compared with the observed tail deformation, and this behavior was attributed to a lack of detail, such as omitted frames and stiffeners. Runtime failures occurred due to instabilities in the LSTC ATD FEMs. The subfloor and tail were modified in terms of detail and mesh refinement which resulted in an increased number of airframe elements from 134,000 to 250,000.

Despite the improvements in the FEM and better qualitative agreement, there were inconsistencies in the accelerometer data. These inconsistencies are highlighted when examining measured and predicted pilot seat box and floor vertical accelerations in

Figure 14. The pilot seat box and floor acceleration pulse shapes and magnitudes both differ between test and analysis. Furthermore, test data show an abrupt spike of 60 to 70 g on the seat box and the floor, most likely from buckling and failure of the keel beam and shear panel under the seat box. This peak is not evident for the predicted seat box response which is approximately 30 g. There is a spike of nearly 50 g in the predicted floor response, but the timing is not coincident. For simplicity, the shell thicknesses are considered constant over the whole region which represents a smeared effective stiffness, whereas the actual hardware has edge doublers and rivets and small cutouts. These simplifying assumptions in the FEM may not account for multiple thin shell buckling and failure modes. This lack of model fidelity is further illustrated by comparing the post-test pilot subfloor photographs to the analysis deformations in Figure 15. From the analysis, plastic deformation occurs along the shear panel and no failure is seen of the keel beam. The post-test photograph indicates a substantial rippled region of the keel beam forward of the shear panel.

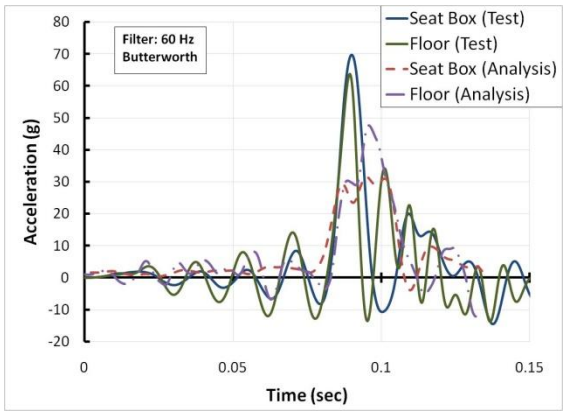

Figure 14. Comparison of test and analysis, pilot seat box and floor vertical acceleration, crash test without DEA

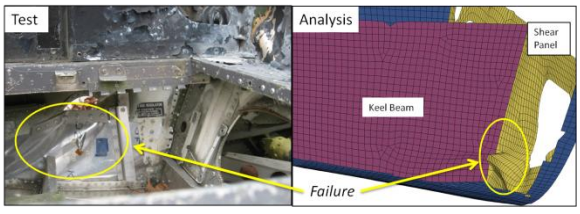

Figure 15. Pilot subfloor: post-test photograph versus analysis

The passenger floor accelerometer is mounted on a relatively stiff interface; thus, local effects are not introduced and the filtered test data tracks better. Comparisons of the passenger floor accelerations are shown in Figure 16. In this case, the passenger floor acceleration compares well in pulse shape and arrival time, but not in magnitude. Furthermore, the predicted pulse shape for the passenger floor is similar to the predicted pilot seat box and pilot floor pulse shapes.

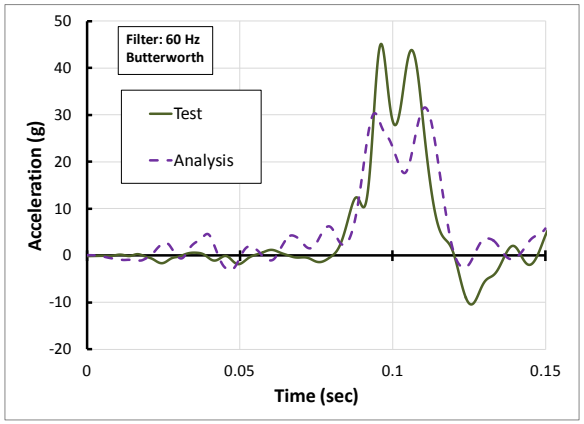

Figure 16. Comparison of test and analysis, passenger floor, vertical acceleration, crash test without DEA

Since the DEA significantly attenuated the impact response during the first crash test, this experimental data may not have been sufficient to validate the analytical model for the subsequent, more severe impact test. The airframe FEM acceleration responses were low and generally in the linear elastic range. The DEA acted as an isolator, accurately imparting loads into the airframe while obscuring deficiencies in the airframe model. These deficiencies became apparent when severe loads and highly nonlinear responses were introduced for the second full-scale test. There are multiple modes of failure in the test without the DEA which may or may not need to be represented by the FEM. From the standpoint of matching acceleration pulse shapes, the FEM detail is adequate in the passenger region, but questionable for the pilot region. The previous assertion of a "validated" FEM based on the crash test with the DEA was questioned. To determine whether more physical detail is required in the model or modification of existing parameters was sufficient to accurately capture responses, a comprehensive calibration was performed.

7. MODEL CALIBRATION BASED ON FULL-SCALE TEST WITHOUT DEA

7.1 Background

The calibration approach adopted for comparison with the second test uses uncertainty propagation and quantification to assess model adequacy. The first step in this approach is parameter selection, which relies heavily on the analyst's knowledge and familiarity with the model and assumptions. After an initial parameter set is selected, uncertainty models to prescribe parameter variations are defined with the aid of empirical data or engineering judgment.

With an initial parameter set and an uncertainty model at hand, parameter importance is assessed using uncertainty propagation. Parameter values in this paper are created using the Halton deterministic sampling technique [19]. Time history results are processed to compute the velocity and acceleration metrics and to assess variability and rank parameters. Adequacy of the parameter set is judged based on the probability of being able to reconcile test with analysis.

Uncertainty propagation is conducted to evaluate uncertainty bounds and to gage the ability of the model to explain the observed behavior. The statistics of the 2-norm of a response vector between test and analysis are compared. An important benefit of using this metric is that it provides for a direct measure of multi-dimensional closeness of two models, with closeness quantified at each time step. Because parameters are uncertain, statistical measures of the metric need to be used to conduct assessments. With limited information about parameter uncertainty, a uniform distribution function, which is the least informative distribution function, is the most appropriate choice to represent parameter uncertainty.

From the perspective of a user, it is important to know the probability of being able to reconcile measured data with predictions, given a particular model for the structure and parameter uncertainty. To this end, let $Q(t,p) \triangleq \|v(t,p)\|_2$ be a scalar time varying function of the 2-norm of the system response vector *v*, using parameter vector *p* at time *t*. Furthermore, let $\underline{\sigma}(t) = \min_{\forall p} Q(t,p)$ be the minimum value over all parameter variations, and let $\overline{\sigma}(t) = \max_{\forall p} Q(t,p)$ be the maximum value. Using these definitions and *N* LS-DYNA solutions, a calibration metric M_1 is used to bound the probability of test values falling outside the analysis bounds;

$$M_1 = Prob\left[\underline{\sigma}(t) < Q_e(t) \vee Q_e(t) \geq \overline{\sigma}(t)\right] \ll \frac{1}{N} \quad (1)$$

where $Q_e(t)$ is the 2-norm of responses from the experiment. Note that *N* controls tightness of the bounds and also the number of LS-DYNA solutions required.

Analysis of variance (ANOVA) is used for parameter sensitivity. In classical ANOVA studies, data is collected from multiple experiments while varying all parameters and also while varying one parameter at a time. These results are then used to quantify the output response variance due to variations of a particular parameter, as compared to the total output variance when varying all the parameters simultaneously. The ratio of these two variance contributions is a direct measure of the parameter importance. Sobol et al. [20] and others [21-23] have studied the problem as a means to obtain global sensitivity estimates using variance-based methods. To compute sensitivity using these variance based methods, one must be able to compute many response predictions as parameters are varied. For this effort, after a suitable set of LS-DYNA solutions are obtained, response surface surrogates are used to estimate additional solutions. The Extended Radial Basis Functions (ERBF) response surface method, as described by Mullur [24,25], is used to estimate time history responses, as opposed to just extreme values.

The use of norms, although convenient, tends to hide the spatial relationships that exist between responses at different locations in the model. In order to study this spatial multi-dimensional dependency explicitly, a different metric must be established. Work by Anderson et al. [26] and Horta et al. [27] proposed the application of singular value decomposition derived basis vectors, or impact shapes. In this approach, time histories from analysis or experiments can be decomposed using singular value decomposition as;

$$y(x,t) = \sum_{i=1}^{n} \sigma_i \phi_i(x) g_i(t) \quad (2)$$

In this form, the impact shape vector ϕ_i sized *m* x 1 contains the spatial distribution information for *m* sensors, $g(t)$ contains the time modulation information, σ contains scalar values with shape participation factors, and *n* is the number of impact shapes to be included in the decomposition, often truncated based on allowable reconstruction error. Although Eq. (2) is written in continuous time form, for most applications, time is sampled at fixed intervals such that $t = k\Delta T$ where the integer k=0,…,L and ΔT is the sample time, and L is the total

number of samples. From Eq. (2), the fractional contribution of the i^{th} impact shape to the total response is proportional to δ_i , defined as;

$$\delta_i = \frac{\sigma_i}{\sum_{l=1}^{n} \sigma_l} \quad (3)$$

Impact shapes can now be used to compare models using orthogonality. Orthogonality, computed as the dot product operation of vectors (or matrices), quantifies the projection of one vector onto another. If the projection is zero, vectors are orthogonal, i.e., distinct. This same idea applies when comparing test and analysis impact shapes. Numerically, the orthogonality metric M_2 is computed as;

$$M_2 = \overline{\Phi}^T \Psi \quad (4)$$

where $\overline{\Phi}$ is sized *m* x *l* with *l* measured impact shapes at *m* locations and Ψ sized *m* x *l* are shapes computed using simulation data. Note that both $\overline{\Phi}$ and Ψ are normalized matrices such that $\overline{\Phi}^T \overline{\Phi} = I$ and $\Psi^T \Psi = I$. Because individual impact shape vectors are stacked column-wise, M_2 is a matrix sized *l* x *l* with diagonal values corresponding to the vector projection numerical value. If vectors are identical then their projection equals 1. Multi-dimensional closeness with experiment is judged based on similarity of impact shapes and shape contributions.

If the model can be reconciled based on both time and spatial calibration metrics, a parameter set is computed which minimizes the squared sum of the prediction error using the Constrained Optimization Response Surface (CORS) optimization scheme of Regis and Shoemaker [28]. Specifically, the algorithm starts by looking for parameter values away from the initial set of LS-DYNA solutions, then slowly steps closer to known solutions by solving a series of locally constrained optimization problems. This optimization process will produce a global optimum if enough steps are taken. The user controls the number of steps and therefore the accuracy and computational expense in conducting the optimization. In cases where the predictive capability of the surrogate model is poor, CORS adds solutions in needed areas. Because parameter uncertainty is not used explicitly in the optimization, this approach is considered to be deterministic.

7.2 Calibration Results

For the purposes of this calibration effort, 19 sensor locations, containing either triaxial or uniaxial accelerometers and totaling 23 channels, were used. At the outset of performing calibration runs, the velocity 2-norm of the sensor set was utilized as a comparison metric. Velocity metrics were used because high frequency responses of structures evident in acceleration time history become naturally filtered once integrated to velocity. Direct comparison between test and analysis velocities is only achievable by integrating the test accelerometer time histories. The integrated test curves are shifted to match to the localized initial velocities that are directly output in the respective local coordinate systems from the analysis. For many of the accelerometers, integration of the signal revealed drifting and inconsistent changes in velocity. The contribution of drift was unique from sensor to sensor and was difficult to detrend. The accelerometers in the calibration sensor set could be successfully integrated and therefore retained.

Altogether, seven different calibration cycles were performed with different parameter sets and varying ranges for each parameter. For the first several calibration cycles, initial conditions were chosen as parameters to vary based on the supposition that there was variability in computing the initial velocities and attitudes from photogrammetry. However, impact conditions such as vertical and horizontal velocities and pitch angle had the highest contribution to the total response variance, which tended to overshadow the importance of structural parameter values. The photogrammetry results were re-examined, and initial conditions permanently fixed.

As calibration cycles were performed, it was also evident that solely using velocity as the comparison metric had a disadvantage. Integration removes critical low- to mid-frequency modes and responses that could be important in identifying shifting load paths as the airframe plastically deforms. Both acceleration and velocity 2-norms were used to determine whether the parameter sets and their range of values were appropriately chosen.

Because of runtime stability issues, the ATD FEM's were removed from the model and their masses evenly distributed onto the seat frames and floor. The ATD FEM model was calibrated independent of the airframe calibration based on results from drop tests of ATD's onto a rigid seat platform [7]. The calibration FEM is shown in Figure 17a, and the calibration sensor locations are shown in Figure 17b.

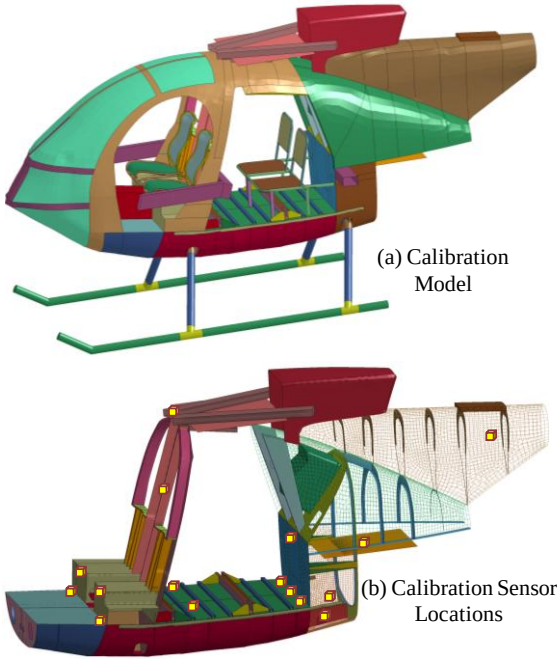

Figure 17. Calibration FEM

Parameter selection for the calibration study addresses two essential aspects of the model, stiffness and plasticity. Most of the critical airframe components in the load path are modeled with shell elements with effective stiffness properties. Seemingly, the thickness of components could be directly measured from the test article. However, the presence of rivets, doublers, and small stiffeners that could not be included in the model without sacrificing computational efficiency would stiffen the test article. Conversely, cutouts and holes would reduce the stiffness. The term "effective" accounts for the omission of these features. To change the effective in-plane and bending stiffness, either the modulus of elasticity or the thickness defined in the shell property can be modified. For this study, the thickness was modified for four structural components, belly thickness, keel beam thickness, seat box thickness, and seat box bulkhead thickness. The airframe is a combination of different alloys of thin sheet or cast aluminum. A fifth parameter, the initial yield stress, was chosen, specifically for parts in the floor and subfloor region where extensive damage occurs.

To illustrate the value of computing the calibration metric M_1, the acceleration and velocity 2-norms are plotted for a set of 60 LS-DYNA runs with five parameters chosen in Figure 18. All acceleration data is low-pass filtered to SAE CFC 60. The test acceleration 2-norms fall outside the bounds provided by the analysis. The velocity 2-norm also indicates that test responses fall outside analytical bounds, but the discrepancy is not as prominent.

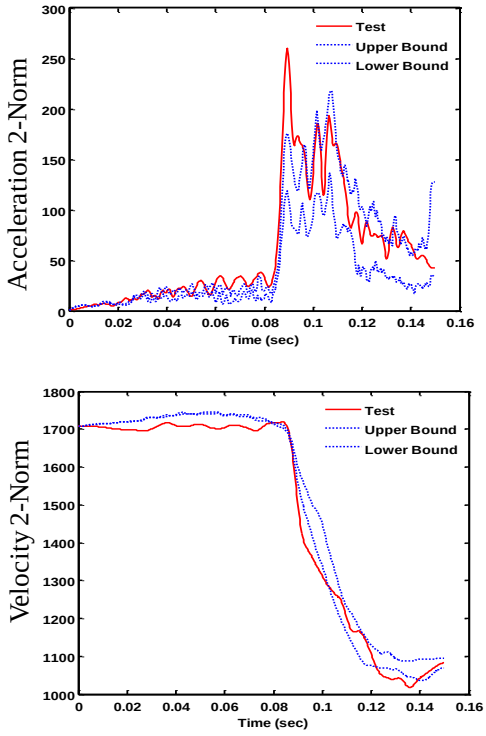

No.	Parameter Description	Nominal	Upper Bound	Lower Bound
1	belly thickness (in)	0.09	0.12	0.08
2	keel beam thickness (in)	0.04	0.07	0.03
3	seat box thickness (in)	0.1	0.12	0.08
4	seat box bulkhead thickness (in)	0.05	0.07	0.03
5	Yield Stress (psi)	40,000	45,000	35,000

Figure 18. Uncertainty bounds for interim calibration cycle

Acceleration results revealed that the time and spatial variation of load transfer is not matched. At the point of belly impact, there are large accelerations in the pilot and copilot region that contribute highly to the 2-norm. Qualitatively, the amount of deformation witnessed from post-test inspection of the subfloor is lower than the analytical predictions. To prevent early yielding and redistribution of loads, the range of probable keel beam thicknesses needed to be increased. This finding is also confirmed from the variance analysis shown in Figure 19. Contribution of a single parameter variance to the total variance was computed throughout calibration cycles to determine whether parameters should be retained or removed from the solution response set. The parameter with

the highest variance contribution immediately following belly impact is the keel beam thickness.

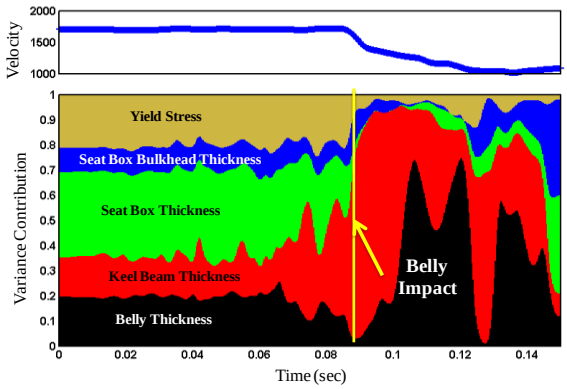

Figure 19. Variance for interim calibration cycle

Calibration runs were conducted with the keel beam thickness increased to a range of 0.10 to 0.15 inches. A total of 60 LS-DYNA runs were performed using the newly defined keel beam parameter range, combined with four other parameters previously defined. Uncertainty bound results for acceleration indicate that the increase in keel beam thickness has shifted the peak acceleration response to align better with the test results. Results in Figure 20 indicate that, based on acceleration and velocity 2-norm, there is a high likelihood that a set of parameters within the range established will reconcile to the test response.

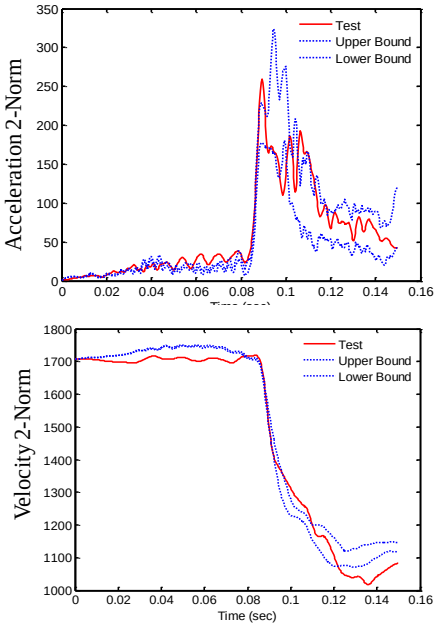

Figure 20. Uncertainty bounds for final calibration cycle

The spatially based metric M_2 was used to perform orthogonality checks between the test and analysis basis vectors. Orthogonality results for the baseline set of parameters and parameters for run 44 are shown in Figure 21. The size of the orthogonality table is equal to the number of impact shapes chosen for both test and analysis *n*. Basis vectors generated from acceleration time histories are compared for test and analysis, with good agreement indicated by the black and dark blue colors. The parameter set of Run #44 (of 60 runs), which is similar to the baseline but has a yield stress nearing the lower bound and a seat box thickness nearing the upper bound, shows improved orthogonality for impact shapes 5 and 6. This does not imply that the selected case is optimal, but it does indicate that slight changes in these parameters can significantly alter the impact shapes.

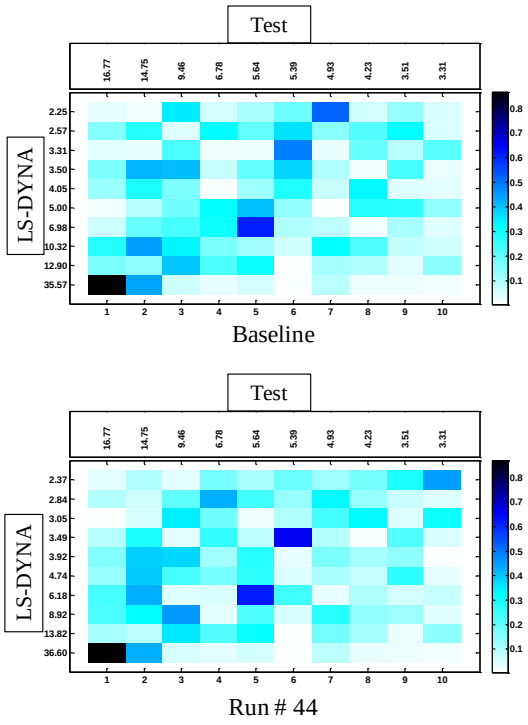

Figure 21. Orthogonality for final calibration cycle

8. RESULTS FOR CALIBRATED MODEL

8.1 Test without DEA

The calibrated set of values for the airframe FEM without the DEA is shown in Table 2. Of the five parameters, three remained close to the nominal value (belly thickness, keel beam thickness, and seat box thickness), while the seat box bulkhead thickness

approached the upper bound, and the yield stress approached the lower bound. This is consistent with the parameters from Run #44.

Table 2. Calibrated parameters

No.	Parameter Description	Nominal	Upper Bound	Lower Bound	Calibrated
1	belly thickness (in)	0.09	0.12	0.08	0.089
2	keel beam thickness (in)	0.12	0.15	0.10	0.12
3	seat box thickness (in)	0.1	0.12	0.08	0.11
4	seat box bulkhead thickness (in)	0.05	0.07	0.03	0.065
5	Yield Stress (psi)	40,000	45,000	35,000	35,210

The updated LSTC Hybrid III ATD FEM is shown in Figure 22. The ATD FEM was calibrated based on vertical drop test data [7]. The first modification performed was mesh refinement. With mesh refinement, the overall contact stiffness on the ATD was improved and the noise present in the original vertical acceleration time histories was eliminated. The original ATD model also had parts in contact with the seat platform that were rigidly represented, which caused peak acceleration readings to rise above reasonable values. The thighs, kneecaps, and feet in the ATD model were re-characterized using deformable material models. A layer of rubber shell elements was overwrapped onto the pelvis and upper thigh parts to represent the skin of the ATD. To represent the abdominal insert that would restrict flailing of the ATD upon impact, linear springs were inserted between the ribcage and the pelvic insert. The spring stiffness was based on the effective material properties of the abdominal insert.

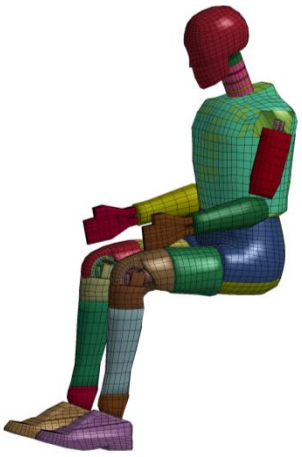

Figure 22. Modified Hybrid III ATD FEM

The original approach of investigating individual acceleration time histories for calibration and validation had been set aside in favor of the uncertainty estimation, parameter sensitivity, and impact shape orthogonality approach. Nonetheless, it is worthwhile to revisit the time histories after modifying the model. The shape, duration and magnitude of acceleration time histories remain important indicators when determining input pulses for seat certification or when evaluating occupant injury criteria such as Eiband, Dynamic Response Index, and Brinkley Index.

The vertical acceleration at the pilot floor is plotted in Figure 23. The overall pulse duration remains about 0.050 seconds. The calibrated model is showing a higher acceleration peak magnitude (60 g) than the original model (47 g), and matches the test peak magnitude better (63 g).

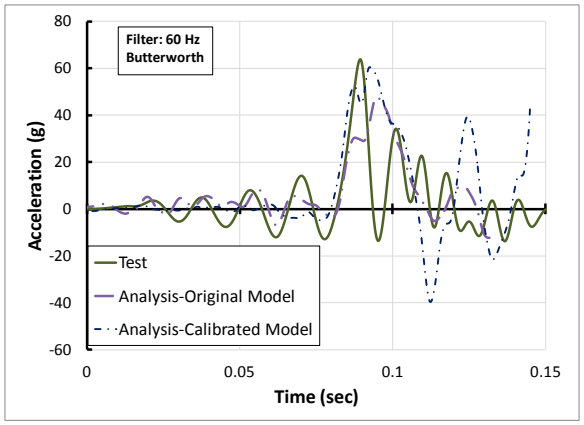

Figure 23. Pilot floor vertical acceleration, crash test without DEA

The passenger floor vertical accelerations are plotted in Figure 24. The analytical waveform shapes and duration agree well with the test, but the peak magnitude of the original model was less than the test acceleration by 15 g. The increase in keel beam stiffness has caused an over-correction in peak magnitude, from 30 g to 70 g. By treating the keel beam as one continuous property, the pilot-copilot region was calibrated properly, but the model behaves too conservatively when examining the passenger region. Hence during calibration, the keel beam area should have been split into separate segments to adjust the areas independently.

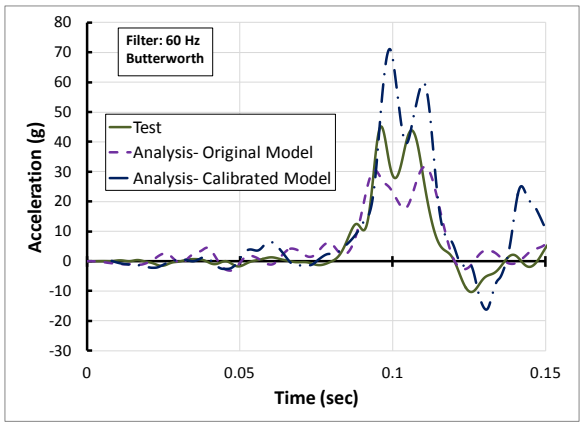

Figure 24. Passenger floor vertical acceleration, crash test without DEA

The pilot pelvic vertical accelerations are plotted in Figure 25. The original model shows a very high pelvic acceleration (140 g), while the calibrated model acceleration was reduced to 100 g. Despite all of the improvements within the ATD FEM, the analysis magnitude exceeds the test magnitude (42 g) by over a factor of two. For both the original and calibrated model, the acceleration spikes could be attributed to the pelvis and seat mesh contacting the seat pan. During post-test inspection, damage was plainly visible on the seat pan, suggesting that contact occurred. However, the spike in load is only evident in the analysis. More modifications are required in the LSTC ATD FEM, further conversion of rigid components to deformable for instance, if results are to be reliably used to evaluate occupant injury.

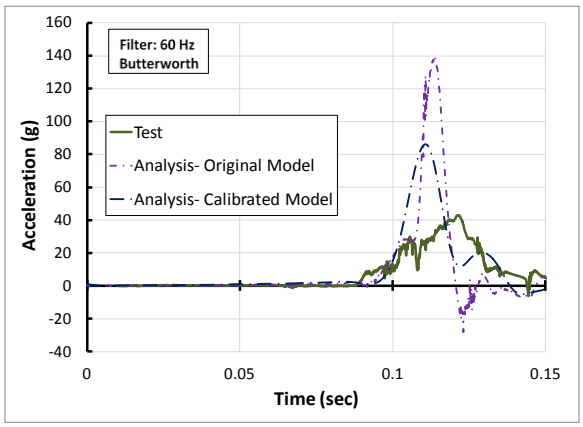

Figure 25. Pilot pelvic vertical acceleration, crash test without DEA

8.2 Test with DEA

The pilot seat vertical accelerations are plotted in Figure 26. The responses for the original and calibrated model are similar in shape and magnitude, with load limiting crush performance of the DEA hovering around 10 g. However, the calibrated model does capture the abrupt rise in acceleration at the end of the pulse. This behavior was not seen with the original model. The stiffening of the subfloor, specifically the keel beam, allowed the compaction phase of the DEA crushing to be transmitted into the cockpit. The passenger floor vertical accelerations in Figure 27 also reveal the similar rise in loads near the end of the pulse.

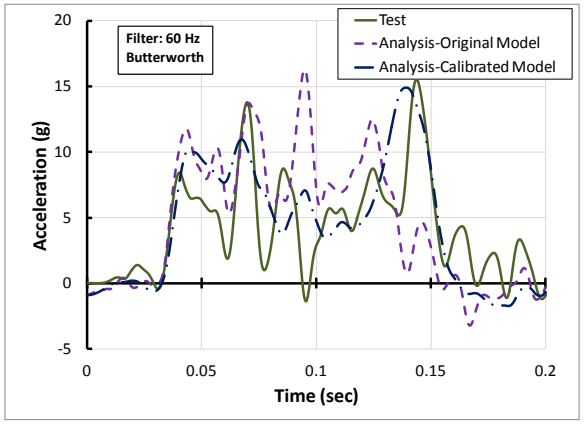

Figure 26. Pilot floor vertical acceleration, crash test with DEA

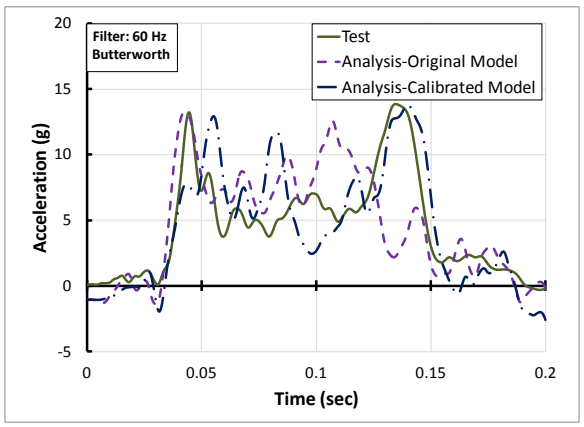

Figure 27. Passenger floor vertical acceleration, crash test with DEA

As shown in Figure 28, the calibrated ATD shows improvement when outputting pelvic vertical accelerations, not unlike the ATD results for the crash test without DEA. The pulse shape is more

flattened and loads are reduced from 25 g to 18 g. Nevertheless, the differences are still significant, and the accuracy of the ATD model is still questionable.

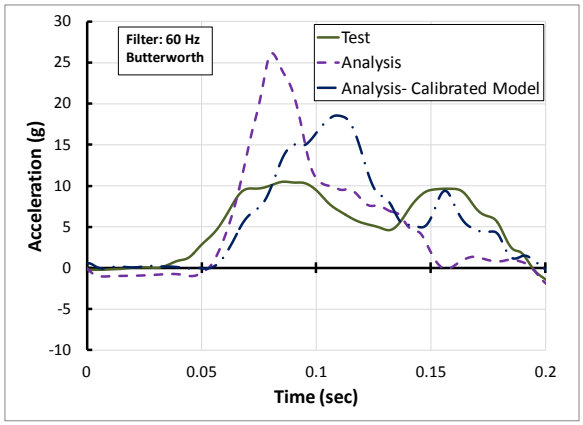

Figure 28. Pilot pelvic vertical acceleration, crash test with DEA

9. CONCLUSION

Results from two full-scale helicopter crash tests have been presented. In the first test a helicopter was fitted with a DEA system, and the second test was conducted without the DEA. Both tests were sponsored by the NASA SRW Program in an effort to evaluate new structural concepts to improve rotorcraft crashworthiness and to increase occupant survivability. The tests demonstrated a peak acceleration reduction upon impact by a factor of three when using the DEA.

Finite element models to predict the overall performance of the rotorcraft were developed and compared to test. Acceleration time histories at the pilot and passenger floor were compared to analysis for both crash tests. Reasonable agreement was seen between test and analysis for the crash test performed with the DEA. The acceleration waveforms and peak values were significantly different between test and analysis for the crash test performed without the DEA. One reason for this discrepancy is the fact that acceleration levels for the test with the DEA were significantly lower and therefore less energy went into deforming the fuselage. Consequently, model fidelity played less of a factor for the test with the DEA.

LS-DYNA model calibration was performed based on two new calibration metrics: (1) a 2-norm velocity bound metric, and (2) orthogonality of test and analysis impact shapes. Results with metric (1) were used to assess the probability of reconciling test with analysis after uncertainty propagation studies. Calibration parameters were selected or removed based on results of metric (1). Orthogonality plots were used to determine if certain parameter sets produced better spatial agreement and clarified stiffness disparities for critical components.

Of consequence to this study, but not previously discussed, are several important considerations when conducting severe crash tests for the purpose of validating analytical models. First, the sensor suite must cover all critical components, and should be mounted on relatively stiff components to avoid high-frequency saturation of the acceleration output. Second, the accelerometers should be calibrated to ensure their velocity integration is accurate. Third, multiple validation metrics should be applied between test and analysis which comprehensively identify modeling deficiencies, evaluate parameter importance, and propose required model changes. Finally, when dealing with very complex structures, a building block approach to model calibration can help break up the problem into more manageable subsystems. The objective of certification by analysis cannot be achieved practically without methodologies established similar to those discussed here.

10. REFERENCES

1. Anonymous, Military Standard, MIL-STD-1290A (AV), Light Fixed- and Rotary-Wing Aircraft Crash Resistance, Department of Defense, Washington DC, 20301, September 26, 1988.
2. Bolukbasi, A., Crocco J., Clarke, C., Fasanella, E., Jackson, K., Leary, P., Labun, L., Mapes, P., McEntire J., Pelletiere, J., Pilati, B., Rumph, F., Schuck, J., Schultz, M., Smith, M., and Vasquez, D., "Full Spectrum Crashworthiness Criteria for Rotorcraft," RDECOM TR 12-D-12, December 2011.
3. AIAA. Guide for the Verification and Validation of Computational Fluid Dynamics Simulations, American Institute of Aeronautics and Astronautics, AIAA-G-077-1998, Reston, VA, 1998.
4. Sprague, M.A., and Geers, T.L., "Spectral Elements and Field Separation for an Acoustic Fluid Subject to Cavitation", Journal of Computational Physics., Vol. 162, 2003, pp. 184-149.
5. Russell, D.M., "Error Measures for Comparing Transient Data: Part I: Development of a Comprehensive Error Measure", Proceedings of the 68th Shock and Vibration Symposium, 2006, pp. 175-184.

6. Horta, L. G., Reaves, M. C., Annett, M. S., Jackson, K. E., "Multi-Dimensional Calibration of Impact Dynamic Models," Proceedings of the IMAC-XXIX Conference and Exposition on Structural Dynamics, Jacksonville, FL, January 31 - February 3, 2011.
7. Polanco, M., and Littell, J. D., " Vertical Drop Testing and Simulation of Anthropomorphic Test Devices," 67th AHS Forum, Virginia Beach, VA, May 3-5, 2011
8. Littell, J. D., "A Comparative Analysis of Two Full Scale MD-500 Helicopter Crash Tests,", Proceedings of the 2010 SEM Annual Conference & Exposition on Experimental and Applied Mechanics, Uncasville, CT, June 2011.
9. Roberts, J., Merkle, A., Biermann, P., Ward, E., Carkhuff, B., Cain, R., and O'Connor, J., "Computational and Experimental Models of the Human Torso for Non-Penetrating Ballistic Impact", Journal of Biomechanics, 40 (1), 2007, pp. 125-136.
10. Jackson, K., Kellas, S, Horta, L.G., Annett, M.S., Polanco, M.A., Littell, J.D., and Fasanella, E.L., "Experimental and Analytical Evaluation of a Composite Honeycomb Deployable Energy Absorber," NASA/TM-2011-217301, November 2011.
11. Hallquist, John Q., "LS-DYNA Keyword User's Manual," Version 971, Livermore Software Technology Company, Livermore, CA, August 2006.
12. Annett, M. S., "LS-DYNA Analysis of a Full-Scale Helicopter Crash Test," 11th International LS-DYNA Users Conference, Dearborn, MI, June 6-8, 2010.
13. Anon, Structural Repair Manual, CSP–SRM–6, MD Helicopters, Inc, Mesa, AZ, May 2006.
14. Polanco, M., "A Parametric Study on a Shell-Based Model of a Kevlar/Epoxy Composite Honeycomb," AHS Technical Specialists Meeting on Rotorcraft Structures and Survivability, Williamsburg, VA, October 27-29, 2009
15. Guha, S., Bhalsod, D., and Krebs, J., "LSTC Hybrid III Dummies, Positioning & Post-Processing, Dummy Version: LSTC.H3.103008_v1.0," LSTC Michigan, October 30, 2008.
16. Eiband, M. A., "Human Tolerance to Rapidly Applied Accelerations: A Summary of the Literature," NASA Memorandum 5-19-59E, June 1959.
17. Brinkley, J.W and Shaffer, J. T., "Dynamic Simulation Tecniques for the Design of Escape Systems: Current Applications and Future Air Force Requirements," *Symposium on Biodynamic Models and their Applications*, AMRL-TR-71-29, Wright-Patterson Air Force Base. Dayton, OH : Aerospace Medical Research Laboratory, 1970.
18. Brinkley, J. W., Specker, L. J.,and Mosher, S. E., "Development of Acceleration Exposure Limits for Advanced Escape Systems," *NATO AGARD Proceedings*, AGARD-CP-472, 1990.
19. Halton, J.H., "On the Efficiency of Certain Quasi-Random Sequences of Points in Evaluating Multi-Dimensional Integrals." *Numerische Mathematik*, Vol. 2, pp. 84-90, 1960.
20. Sobol, I.M., Tarantola, S., Gatelli, D., Kucherenko, S.S, and Mauntz, W.: "Estimating Approximation Error When Fixing Unessential Factors in Global Sensitivity Analysis." Reliability Engineering and System Safety 92, pp. 957-960, 2007.
21. Mullershon, H., and Liebsher, M.: "Statistics and Non-Linear Sensitivity Analysis with LS-OPT and DSPEX." Proceedings of the10th International LS-DYNA Users Conference, Dearborn, MI, pp. 4-1,4-13, June 8-10, 2008.
22. Homma, T, and Saltelli, A., "Importance Measures in Global Sensitivity Analysis of Nonlinear Models." Reliability Engineering and System Safety 52, pp. 1-17, 1996.
23. Sudret, B., "Global Sensitivity Analysis Using Polynomial Chaos Expansion." Reliability Engineering and System Safety 93, pp. 964-979, 2008.
24. Mullur, A. and Messac, A., "Extended Radial Basis Functions: More Flexible and Effective Metamodeling." AIAA Journal, Vol., 43, No. 6, June 2005.
25. Mullur, A. and Messac, A.: "Metamodeling Using Extended Radial Basis Functions: A Comparative Approach." Engineering with Computers,Vol. 21: pp.203-217, 2006.
26. Anderson, M.C., Gan, W., and Hasselman, T.K., "Statistical Analysis of Modeling Uncertainty and Predictive Accuracy for Nonlinear Finite Element Models." Proceedings of the 69th Shock and Vibration Symposium, Minneapolis/St. Paul, MN, 1998.
27. Horta, L.G., Lyle, K.H., Lessard, W.B., "Evaluation of Singular Value Decomposition Approach for Impact Dynamic Data Correlation." NASA TM 2003-212657, Oct. 2003.
28. Regis, R.G., and Shoemaker, C.A., "Constrained Global Optimization of Expensive Black Box Functions Using Radial Basis Functions." Journal of Global Optimization, Vol. 31: pp. 153-171, Sept. 2005.